How to cite: *Angew. Chem. Int. Ed.* **2022,** *61,* e202209075
International Edition: doi.org/10.1002/anie.202209075
German Edition: doi.org/10.1002/ange.202209075

VIP **Hydrogen Evolution** **Very Important Paper**

Unravelling the Mechanistic Pathway of the Hydrogen Evolution Reaction Driven by a Cobalt Catalyst

Bing Jiang, Marcos Gil-Sepulcre, Pablo Garrido-Barros, Carolina Gimbert-Suriñach, Jia-Wei Wang, Jordi Garcia-Anton, Pau Nolis, Jordi Benet-Buchholz, Nuria Romero,* Xavier Sala,* and Antoni Llobet*

Abstract: A cobalt complex bearing a κ-N_3P_2 ligand is presented ($\mathbf{1}^+$ or Co^I(L), where L is (1*E*,1′*E*)-1,1′-(pyridine-2,6-diyl)bis(*N*-(3-(diphenylphosphanyl)propyl)ethan-1-imine). Complex $\mathbf{1}^+$ is stable under air at oxidation state Co^I thanks to the π-acceptor character of the phosphine groups. Electrochemical behavior of $\mathbf{1}^+$ reveals a two-electron Co^I/Co^{III} oxidation process and an additional one-electron reduction, which leads to an enhancement in the current due to hydrogen evolution reaction (HER) at $E_{onset} = -1.6$ V vs Fc/Fc^+. In the presence of 1 equiv of bis(trifluoromethane)-sulfonimide, $\mathbf{1}^+$ forms the cobalt hydride derivative Co^{III}(L)-H ($\mathbf{2}^{2+}$), which has been fully characterized. Further addition of 1 equiv of $CoCp^*_2$ (Cp* is pentamethylcyclopentadienyl) affords the reduced Co^{II}(L)-H ($\mathbf{2}^+$) species, which rapidly forms hydrogen and regenerates the initial Co^I(L) ($\mathbf{1}^+$). The spectroscopic characterization of catalytic intermediates together with DFT calculations support an unusual bimolecular homolytic mechanism in the catalytic HER with $\mathbf{1}^+$.

Introduction

Hydrogen fuel production via proton reduction ($2H^+ + 2e^- \rightarrow H_2$) is considered a promising method to generate a renewable and highly energetic fuel in a sustainable manner. Homogeneous molecular catalysts have been actively investigated, largely due to the wealth of mechanistic information that these well-defined systems can offer. The use of cobalt complexes to mediate this two electron reduction process has experienced a significant progress in the last fifteen years giving rise to a broad family of highly active compounds that take advantage of the versatility of ligand design to tune the electronic, steric and second coordination effects in the catalytic process.[1–8] One of the key aspects that has enabled the improvement of the catalytic performance is the possibility to study the mechanism of the reaction through static and time-resolved spectroscopic techniques that allow to follow the kinetics of the process as well as the detection and characterization of intermediate species.[9–22] Theoretical calculations have also contributed in the understanding and supporting of the experimental findings.[23–25] From these studies, it derives that a reduced formal Co^I species is required to trigger the catalytic process. The latter can react with a proton to generate a cobalt (III) hydride species (Co^{III}-H) that is an important intermediate in the catalytic cycle from which hydrogen can evolve. Alternatively, the Co^{III}-H can be reduced to its Co^{II}-H derivative that can also lead to hydrogen generation. For many highly active catalysts, these hydride species remain elusive because of their high reactivity. Only a few examples reported in the literature give experimental evidence for the formation of such cobalt-hydride[3,13,18,22] and other metal-hydride[26–31] species as actual hydrogen evolving intermediates. Of special interest is also the elucidation of the mechanism by which those metal hydrides operate towards formation of an H–H bond, predominantly involving pathways first order in either Co^{III} or Co^{II} hydride species. Examples of bimolecular HER from first-row transition metal hydrides are still limited.[32–41]

In this work we isolate and characterize a Co^{III}(L)-H compound derived from a Co^I(L) complex, which is a key intermediate towards the hydrogen evolution reaction. The cobalt complexes have a neutral pentadentate ligand (L)

[*] Dr. B. Jiang, Dr. C. Gimbert-Suriñach, Dr. J. Garcia-Anton, Dr. N. Romero, Dr. X. Sala, Prof. A. Llobet
Departament de Química, Universitat Autònoma de Barcelona
Cerdanyola del Valles, 08193 Barcelona (Spain)
E-mail: xavier.sala@uab.cat

Dr. M. Gil-Sepulcre, Dr. P. Garrido-Barros, Dr. C. Gimbert-Suriñach, Dr. J.-W. Wang, Dr. J. Benet-Buchholz, Prof. A. Llobet
Institute of Chemical Research of Catalonia (ICIQ),
Barcelona Institute of Science and Technology (BIST)
Av. Països Catalans 16, 43007 Tarragona (Spain)
E-mail: mgil@iciq.es

Dr. P. Nolis
Servei de Ressonància Magnètica Nuclear,
Universitat Autònoma de Barcelona
08193 Bellaterra, Barcelona, Catalonia (Spain)

Dr. N. Romero
Laboratoire de Chimie de Coordination (LCC)—UPR 8241
205 Route de Narbonne, BP44099,
31077 Toulouse Cedex 4 (France)
E-mail: nuria.romero@lcc-toulouse.fr

based on the redox active 2,6-bis(imino)pyridine scaffold with two phosphine arms (L = (1*E*,1′*E*)-1,1′-(pyridine-2,6-diyl)bis(*N*-(3-(diphenylphosphanyl)propyl)ethan-1-imine). The former has shown the capability of storing multiple electrons,[42–48] assisting reductive catalysis, while the π-acceptor nature of the phosphine groups in L lower the electron density on the metal potentially reducing reduction potentials for the HER.

Results and Discussion

Synthesis and Structural Characterization of 1^+

Complex $[Co^{I}(L)]^+$ ($\mathbf{1}^+$) was prepared by mixing the N_3P_2 ligand (1*E*,1′*E*)-1,1′-(pyridine-2,6-diyl)bis(*N*-(3-(diphenylphosphanyl)propyl)ethan-1-imine)[49,50] with $Co^{II}(BF_4)_2{\cdot}6H_2O$ in tetrahydrofuran at room temperature. After stirring for 1 day, the dark black-green solution was dried under vacuum and the resulting powder re-dissolved in a dichloromethane/methanol mixture. Layering with pentane afforded black crystals of $\mathbf{1}BF_4$ resulting in a 26% of total yield (see Experimental section in the Supporting Information).[51] Complex $\mathbf{1}^+$ is stable under air in the solid state in contrast to related Co^{I} complexes bearing the 2,6-bis(imino)pyridine ligand,[15,20,21,48] highlighting the π-accepting character of the two extra phosphine moieties, which stabilize the low-valent metal center. Compound $\mathbf{1}^+$ has been fully characterized by ESI mass spectrometry, single crystal X-ray diffraction, NMR and UV/Vis spectroscopies as well as cyclic voltammetry (CV). The ESI-MS spectrum confirmed the presence of the cation $\mathbf{1}^+$ at $m/z = 672.1$ and the double charged $[Co^{II}(L)\text{-}MeOH]^{2+}$ species at $m/z = 352.1$, formed under the ESI conditions (Figure S17).

The crystal structure of $\mathbf{1}^+$ belongs to a $P2(1)/n$ monoclinic space group. The cobalt center is five coordinated with three N atoms and two P atoms from the pentadentate ligand (Figure 1), where the metal is closer to a distorted trigonal-bipyramidal environment, with the pyridine nitrogen atom and two phosphorus atoms forming the equatorial plane and two imine nitrogen atoms occupying the axial positions. The angles of the trigonal plane, P(1)–Co(1)–P(2) = 111.27°, N(2)–Co(1)–P(2) = 123.53° and N(2)–Co(1)–P(1) = 125.19°, deviate somewhat from the ideal trigonal angle of 120°. However the sum of these angles is 360°, confirming the planarity of the trigonal plane that is composed of N(2), P(1) and P(2) atoms. The solid-state structure determined by X-ray crystallography displays a monocationic complex with the presence of only one BF_4^- as counterion. This is in agreement with the resulting elemental analyses and suggests that a disproportion of the corresponding Co^{II} species, formed from the $Co^{II}(BF_4)_2{\cdot}6H_2O$ precursor, takes place during the synthetic procedure (see electrochemistry below). Taking into account the redox non-innocent character of the bis(imino)pyridine chelate, the electronic configuration of $\mathbf{1}^+$ can be described as a low valent Co^{I} ion stabilized by the neutral ligand, or can be regarded as a Co^{II} ion antiferromagnetically coupled to a ligand radical anion. Inspecting the imine C=N

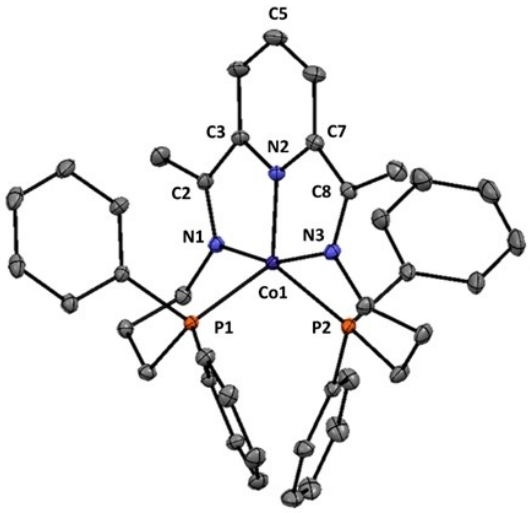

Figure 1. ORTEP drawing of $\mathbf{1}^+$ with 50% probability thermal ellipsoids. Hydrogen atoms and counter ions have been omitted for clarity. Color code: Carbon (grey), Nitrogen (Blue), Phosphorous (orange) and Cobalt (purple).

distances, a moderate elongation (1.3263(9) and 1.3256(9) Å compared to unreduced bis(imino)pyridine ligands 1.28 Å) is observed in both cases. Moreover, the C_{im}–$C_{py(o)}$ bond lengths (1.4449(10) and 1.4405(10) Å), that is C(2)–C(3) and C(8)–C(7) in Figure 1, are obviously contracted relative to neutral chelates (1.50 Å).[42,47] Even if these metrical parameters may imply a reduced bis(imino)pyridine chelate as monoanion, we cannot determine this conclusion without further evidence. For instance, similar bond elongation and contraction observed in a manganese complex with the formula $[Mn^{I}(PDI)(CO)]^+$ (PDI is pyridyl(diimine)) has been attributed to Mn-to-PDI, back-bonding rather than to the reduction on redox-active ligand through Density Functional Theory (DFT) calculations.[46,50] Likewise, in this case, DFT calculations resulted in the most stable singlet configuration corresponding to a Co^{I} complex with a consistent trigonal-bipyramidal coordination environment, although with less than 1 kcal mol^{-1} difference from the corresponding triplet configuration revealing the close proximity of both electronic structures. Similar to the $[Mn^{I}(PDI)(CO)]^+$ system, analysis of the HOMO, which is mainly centered in the metal d orbitals, evidences partial contribution of the π-orbitals from the bis(imino) ligand that can also be explained as strong back-bonding interactions (Figure S24).

Compound $\mathbf{1}^+$ is a diamagnetic compound and has been fully characterized by 1D and 2D NMR spectroscopy in CD_2Cl_2 (Figure S1–S6). These analyses indicate the symmetric character of $\mathbf{1}^+$ which belongs to the C_2 point group in solution, with the rotational axis passing through C(5), the N(2) atom of the pyridine ring, and the central Co atom. A singlet at 43.2 ppm appears in the $^{31}P\{^1H\}$ NMR spectrum, typical chemical shift range for coordinated phosphorus donor atoms.[49] The ^1H NMR spectrum shows six methylene resonances, which contrasts to the three resonances displayed by the free ligand. In addition to the propyl-bridged chelate arms, long range ^{31}P-coupling to the bis(imino)-

pyridine backbone methyl (H5, t, 6H) and *p*-pyridine (H1, tt, 1H) resonances at 2.27 and 8.08 ppm, respectively, were also observed (Figure S1, insets). $\mathbf{1}^+$ also differs from the parent free ligand in the splitting of the resonances corresponding to the phenyl substituents on the P atoms, showing six signals in the 7.55 to 6.12 ppm range instead of three, due to the loss of symmetry of the phenyl moieties upon coordination.

The electronic absorption spectrum of $\mathbf{1}^+$ in acetonitrile shows two intense characteristic absorption bands in the UV region at $\lambda = 260$ nm ($\varepsilon = 33\,000\ M^{-1}cm^{-1}$) and $\lambda = 317$ nm ($\varepsilon = 11\,000\ M^{-1}cm^{-1}$), which are assigned to ligand-based $\pi \rightarrow \pi^*$ transitions (Figure S18). In the visible region, $\mathbf{1}^+$ displays a band of medium intensity at $\lambda_{max} = 432$ nm ($\varepsilon \approx 16\,000\ M^{-1}cm^{-1}$), attributed to metal to ligand charge transfer (MLCT). In addition, two broad absorption bands with relatively low intensity ($\varepsilon \approx 3000\ M^{-1}cm^{-1}$) are observed at 498–611 nm and 611–800 nm, more likely resulting from d–d transitions. Similar broad bands in the same spectral region have been reported for related Co^I compounds.[10,15,52]

Electrochemical Analysis of 1^+

The redox properties of $\mathbf{1}^+$ were studied by cyclic voltammetry. As shown in Figure 2a, the CV of $\mathbf{1}^+$ in dry DMF (0.1 M nBu_4NPF_6 solution) features two reversible waves at $E^1_{1/2} = -2.02$ V ($\Delta E_p = 79$ mV) and $E^2_{1/2} = -0.24$ V ($\Delta E_p = 112$ mV), all potentials reported in this manuscript have been measured using a $Ag/AgNO_3$ (0.01 M $AgNO_3$ in acetonitrile containing 0.1 M nBu_4NPF_6) reference electrode and have been converted to Fc/Fc^+ by adding ferrocene as internal standard at the end of the experiments.

The first wave at E^1 is tentatively assigned to the ligand based $L^{0/\bullet-}$ couple, thus generating $Co^I(L^{\bullet-})$ species (**1**) upon one-electron reduction. This is also supported by DFT calculations showing the LUMO of the $\mathbf{1}^+$ complex being centered in the bis(imino)pyridine ligand (Figure S24). Consistently, the optimized one-electron reduced species features a doublet electronic configuration with a SOMO corresponding to ligand π-orbitals, with a calculated redox potential of −1.92 V that is in good agreement with the observed experimental value (Figures S25 and S26).

The wave observed at $E^2_{1/2} = -0.24$ V integrates twice as compared to E^1 (80.4 vs 39.7 μC) and is attributed to the two-electron oxidation of $\mathbf{1}^+$ to form the corresponding Co^{III}(L)-S complex ($\mathbf{3}^{3+}$, where S is DMF or MeCN depending on the utilized solvent), due to a disproportionation of the transient intermediate Co^{II}(L)-S species. This oxidative event was also studied by DFT in order to elucidate the nature of the two-electron oxidation and results are summarized in Figures S27–S29. Computationally, one-electron oxidation of the Co^I(L) complex leads to a Co^{II}(L) species with a distorted square pyramidal geometry and a high spin, quartet configuration, which is close in energy to the low-spin, doublet configuration. Interestingly, the large geometric rearrangement upon oxidation exposes a vacant site in the Co^{II}(L) metal center that is now accessible. Coordination of a solvent molecule in this oxidation state is slightly endothermic according to the standard free energy, $\Delta G^\circ = 5.9$ kcal mol^{-1}, suggesting its plausible coordination using DMF as the solvent. When the corresponding oxidized Co^{III}(L) complex is considered, coordination of a DMF molecule at the vacant position is now thermodynamically favorable according to ΔG°, leading to an octahedral coordination environment forming the complex Co^{III}(L)-S ($\mathbf{3}^{3+}$) (Figure S28). The structure rearrangement and the coordination event trigger the disproportionation reaction according to the calculated $\Delta G^\circ = -1.9$ kcal mol^{-1} for the overall process (Figure S29).[53] This reactivity also explains the observed disproportionation process during the synthetic procedure, where either the water molecules in the starting material, $Co(BF_4)_2{\cdot}6H_2O$, or the methanol solvent from recrystallization might promote coordination and oxidation to the corresponding Co^{III} complex.

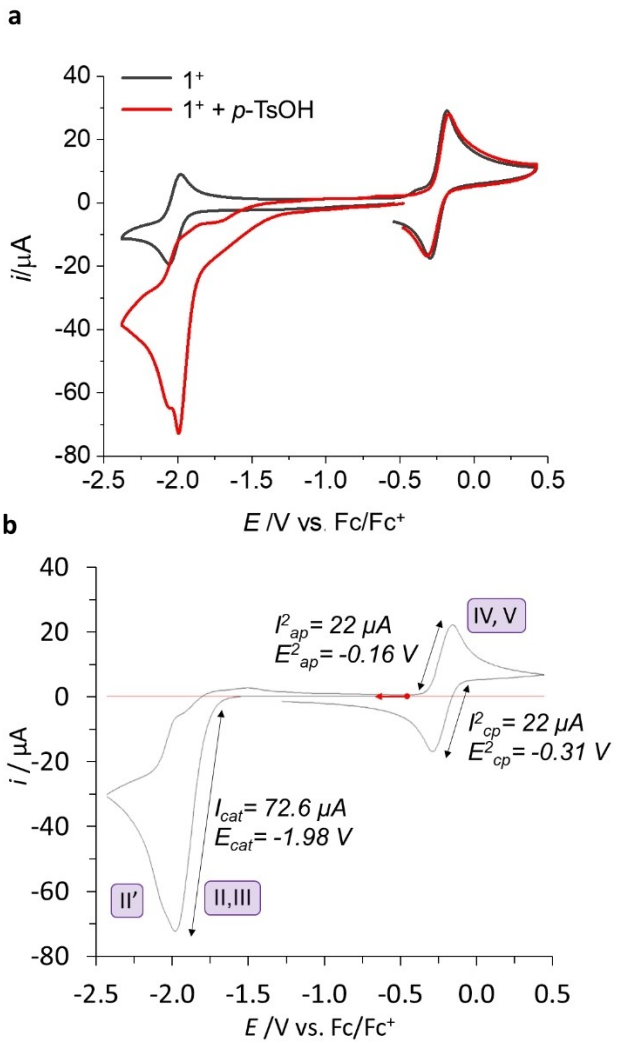

Figure 2. a) Cyclic voltammograms of 1 mM $\mathbf{1}^+$ in 0.1 M nBu_4NPF_6 DMF in the absence (black line) and presence (red line) of 5 mM *p*-TsOH at scan rate of 100 mV s^{-1}. b) Simulated cyclic voltammogram of 1 mM solution of $\mathbf{1}^+$ in presence of 5 mM *p*-TsOH in 0.1 M nBu_4NPF_6 DMF at scan rate of 100 mV s^{-1}. CV obtained by means of *DigiSim 2.0 CV* simulator software using the proposed mechanistic model in Scheme 2.

The oxidation of $\mathbf{1}^+$ was studied chemically by employing stoichiometric amounts of an oxidizing reagent, ferrocenium tetrafluoroborate ($FcBF_4$), causing a color change from dark green-brown to orange immediately. The reaction was monitored by UV/Vis and ^{1}H NMR spectroscopy (Figure S19 and Figure S7, respectively). With regards to UV/Vis spectroscopy, a new band at 379 nm appeared while the bands at 434 nm, 498–611 nm and 611–800 nm vanished upon adding aliquots of $FcBF_4$ showing isosbestic points at 283 nm and 411 nm. The ^{1}H NMR spectrum of the resulting species (Figure S7) shows a new diamagnetic species attributed to Co^{III}(L)-S ($\mathbf{3}^{3+}$). This species displays significantly altered chemical shifts with regard to its parent $\mathbf{1}^+$ derivative, such as the representative *m*-pyridine doublet resonance at 8.37 ppm in $\mathbf{1}^+$ shifted to higher field (7.88 ppm) or the *p*-pyridine triplet of triplets at 8.07 ppm moved to lower field (8.17 ppm). In addition, the resonances of phenyl protons shift to lower fields and to a narrower chemical shift range (6.76–7.79 ppm).

Reactivity of $\mathbf{1}^+$ under Electrocatalytic Proton Reduction Conditions

As shown in the cyclic voltammogram of Figure 2a, when *p*-toluenesulfonic acid (*p*-TsOH, $pK_a = 2.6$ in DMF)[54] is added to a DMF solution of $\mathbf{1}^+$, a significantly different profile is observed in its reduction chemistry. When scanning to the cathodic direction, an irreversible wave starting at $E_{onset} = -1.6$ V is observed, followed by a sharp current increase assigned to the electrocatalytic hydrogen evolution reaction. The shift of the first reduction accounts for more than 200 mV when compared to pure complex $\mathbf{1}^+$ and indicates that a different species is responsible for this redox process. Additionally, the presence of the Co^I(L)/Co^I($L^{\bullet-}$) redox feature at $E^1_{ap} = -2.04$ V also in the presence of a proton source suggest the existence of an equilibrium between initial species in solution, $\mathbf{1}^+$, and the new formed species that we attribute to the hydride derivative Co^{III}(L)-H, $\mathbf{2}^{2+}$ (process A in Scheme 1). This species can be formed after the reaction of $\mathbf{1}^+$ with a H^+, where the Co^I center contributes with two electrons to form the Co–H bond. Interestingly, the oxidation signature corresponding to the Co^{III}(L)-S/Co^I(L) couple is unaltered, suggesting that the new species converts to the original complex $\mathbf{1}^+$ after scanning through the catalytic process, which remains as the resting state. The electrocatalytic formation of hydrogen was confirmed by a controlled potential electrolysis (CPE) experiment of a solution of $\mathbf{1}^+$ at $E_{app} = -2.0$ V carried out in a gas-tight two-compartment electrochemical cell equipped with a Clark-type electrode to monitor hydrogen evolution in the headspace. Thereby, a fairly stable current profile (*i* vs *t*) was observed during 1 hour of experiment achieving a TON of 8.7 and a Faradaic efficiency of 84 % (Figure S32).

The electrochemical scenario in the absence and in the presence of proton source was investigated by simulating the experimental CV recorded at 100 mV s^{-1} by an iterative mathematical process using the Digisim 2.0 CV simulator software to get insights into kinetic (*k*) and thermodynamic (*K*) constants of the processes. Figure 2b shows the resulting simulated CV, which matches with the electrochemical response of $\mathbf{1}^+$ in the presence of *p*-TsOH in DMF (see also Figures S33 and S34). As discussed above, the shift of the onset of first reduction wave observed in the presence of a proton source suggests a first non-faradaic intramolecular redox event that involves the formation of Co^{III}(L)-H species, $\mathbf{2}^{2+}$, coexisting with $\mathbf{1}^+$ in solution (A in Scheme 1, I in Scheme 2). This equilibrium was calculated and resulted to be shifted towards the formation of hydride species ($K_{eq} = 1800$) with a kinetic constant of $k^1 = 2.5 \times 10^{-2}$ M^{-1} s^{-1}. Afterwards, an electron transfer process takes place to Co^{III}(L)-H, $\mathbf{2}^{2+}$, with the SOMO being partially delocalized over the bis(imino)pyridine backbone, the metal center and the hydride to generate a formal Co^{II}(L)-H ($\mathbf{2}^+$) as supported by DFT calculations (see below) and triggering the hydrogen evolution reaction (D in Scheme 1 and II in Scheme 2). Interestingly, CV simulations match with the formation of hydrogen through a homolytic mechanism, which involves the interaction of two Co^{II}(L)-H units to form the H–H bond (F in Scheme 1 and III in Scheme 2). A second-order kinetic constant of $k_{cat} = 7 \times 10^3$ M^{-1}s^{-1} was obtained for the catalytic process, which perfectly reproduces the experimentally observed cathodic potential and

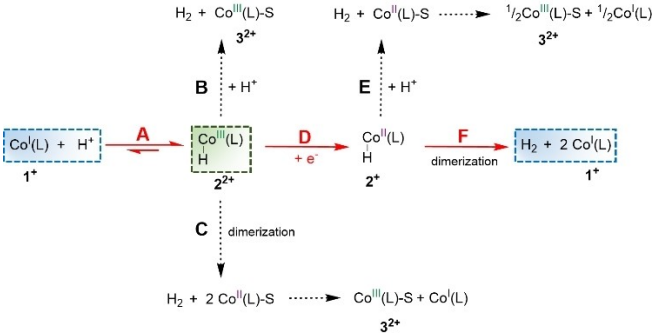

Scheme 1. Mechanistic hydrogen evolution pathways from the Co^I(L) complex $\mathbf{1}^+$. The mechanistic pathway followed by $\mathbf{1}^+$ is highlighted (red arrows), the highlighted squares indicate the isolated and characterized compounds in this work.

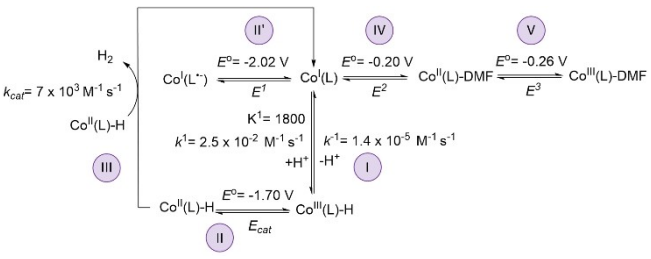

Scheme 2. Proposed scenario for electrochemical reduction and oxidation reactions of complex $\mathbf{1}^+$ in presence of a proton source in DMF. The scheme shows the potentials ($E°$), kinetic (*k*) and thermodynamic (*K*) constants utilized for simulating the cyclic voltammogram shown in Figure 2 by *DigiSim 2.0 CV*.

current ($E_{cat}=-1.98$ V and $I_{cat}=72.6$ μA, respectively). Simultaneously, non-reacted Co^{I}(L), $\mathbf{1}^{+}$, can be reduced to $Co^{I}(L^{\bullet-})$, **1**, at a more negative potential ($E^{I'}=-2.04$ V, process II′). Finally, the Co^{III}(L)-S/Co^{I}(L) feature was simulated in the subsequent anodic scan as a two-electron wave resulting from the disproportion of the formed Co^{II}-(L)-S species (IV and V in Scheme 2).

CVs of $\mathbf{1}^{+}$ performed in the presence of a stronger acid trifluoromethanesulfonimide (TFSI, $pK_a=-11.9$ in 1,2-dichloroethane),[55] show a sharp increase of the current at $E_{onset}=-1.6$ V, matching with the catalytic process observed with *p*-TsOH (Figure S36). Interestingly, the precatalytic process observed at $E_{onset}=-1.4$ V is not present, and therefore, it could be potentially attributed to an electron transfer process related with the *p*-TsOH.[56] At the anodic scan, a clear decrease in the intensity of the Co^{III}(L)-S/Co^{I}(L) feature is observed, which suggests a faster formation of the Co^{III}(L)-H in the presence of TFSI during the short timescale of the CV. Additionally, the dependence of the intensity of the catalytic process, located at $E_{cat}=-1.98$ V, with the concentration and the scan rate was investigated. The plot of I_{cat} vs [$\mathbf{1}^{+}$] clearly shows a linear dependence of the catalytic process with the concentration of $\mathbf{1}^{+}$, which confirms that the rate determining step (rds) for the hydrogen evolution reaction is taking place before the interaction of two Co^{II}(L)-H units to form the H–H bond, most likely during the formation of Co^{III}(L)-H or the reduction to form the Co^{II}(L)-H. The experimental trend matches with the mechanistic model proposed by CV simulations at different catalyst concentrations, which reproduces the linear relationship between I_{cat} and [$\mathbf{1}^{+}$] (Figure S35). Additionally, an enhancement of the current centred at the Co^{I}(L)/$Co^{I}(L^{\bullet-})$ redox feature ($E=-2.04$ V, Figure S37) is observed when $\mathbf{1}^{+}$ does not consume all the protons in the double layer, evidencing catalysis also gated by this couple (CVs performed at fast scan rates and low catalyst concentration, Figure S37). In the electrocatalytic event the main process is dominated by the reduction of Co^{III}(L)-H ($\mathbf{2}^{2+}$) to the active Co^{II}(L)-H ($\mathbf{2}^{+}$) species. However, the Co^{I}(L)/$Co^{I}(L^{\bullet-})$ couple can become important in the catalytic process at lower potentials, through the binding of a H^{+} forming the Co^{II}(L)-H intermediate. The latter is the species capable of producing hydrogen via the homolytic mechanism described herein.

Spectroscopic Characterization of the Cobalt Hydride 2^{2+} Intermediate

To further investigate the processes observed during the electrochemical studies with $\mathbf{1}^{+}$, UV/Vis and NMR spectroscopies were utilized to monitor and characterize the species generated from $\mathbf{1}^{+}$ in the presence of *p*-TsOH. The evolution of the electronic spectra is shown in Figures S20 and S21 in acetonitrile and DMF, respectively. In acetonitrile, the band at 432 nm and the broad bands at 482–600 nm and 600–800 nm decreases gradually while a new band at 379 nm appears. The process is slow and incomplete after prolonged reaction times, but it proceeds with isosbestic points at 357 nm and 397 nm, which indicate a clean transformation between the initial and final species.

The ^{1}H NMR spectrum in CD_3CN shows the gradual growing of a triplet at −9.43 ppm (with $J_{H\text{-}P}=57$ Hz) upon addition of the acid, indicating that a diamagnetic cobalt hydride is generated in the presence of *p*-TsOH (Figure 3a). Consistent with the UV/Vis and electrochemical experiments discussed above, the NMR analysis confirms the slow formation of Co^{III}(L)-H, $\mathbf{2}^{2+}$, with only partial conversion of the initial Co^{I}(L) complex, $\mathbf{1}^{+}$. A careful inspection on the aryl region of the spectrum reveals eight new generated resonances (highlighted in Figure 3a), which coincides with the number of resonances of the parent complex $\mathbf{1}^{+}$. The $^{31}P\{^{1}H\}$ NMR spectrum displays two peaks, the first corresponding to the initial Co^{I}(L) complex and a second one at 36.5 ppm corresponding to the new Co^{III}(L)-H species (Figure S8). Taking all the information into account, a symmetric structure is proposed in Figure 3b, with a κ^5-*N*,*N*,*N*,*P*,*P*-coordination by the pentadentate ligand and the hydrido ligand occupying a putative axial position of an octahedral type of geometry. This is further supported by DFT calculations, where a singlet Co^{III}(L)-H hydride species is optimized with an octahedral geometry upon coordination of a proton to the initial Co^{I}(L) complex. Considering *p*-TsOH as the acid, the calculated free energy of the Co^{III}(L)-

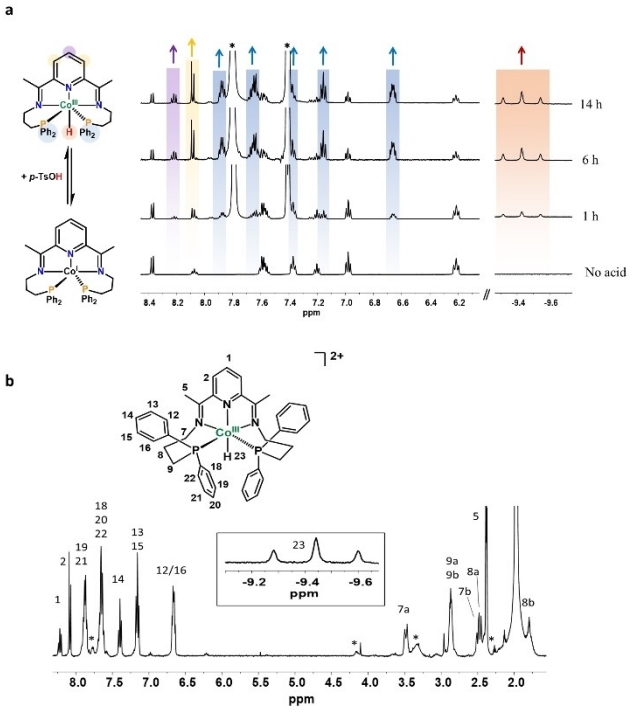

Figure 3. a) ^{1}H NMR spectra (500 MHz, CD_3CN, 298 K) of $\mathbf{1}^{+}$ (bottom line) and in situ generation of the corresponding Co^{III}(L)-H, $\mathbf{2}^{2+}$, derivative upon the addition of 25 equiv *p*-TsOH in CD_3CN, after 1 h, 6 h (middle lines) and 14 h (top line), presenting the aromatic region resonances and amplified triplet corresponding to the hydride at −9.43 ppm, arrows indicate the growing of new signals attributed to $\mathbf{2}^{2+}$. b) ^{1}H NMR spectra of $\mathbf{2}^{2+}$ (400 MHz, CD_3CN, 298 K) recorded immediately after excess TFSI was added to the Co^{I}(L) complex, $\mathbf{1}^{+}$. * Unidentified species formed after the addition of TFSI.

H formation is $\Delta G_{calc} = -1.5$ kcal mol^{-1}, which is only slightly exothermic (Figure S30), in agreement with the experimentally observed equilibrium character of this reaction.

Full spectroscopic characterization of the cobalt hydride was achieved by using a stronger acid to push the reaction to completion, using trifluoromethanesulfonimide. Thus, full assignment of the ^{1}H NMR spectrum of $\mathbf{2}^{2+}$ was achieved by combined 1D and 2D experiments (Figure 3b and Figures S9–S11). It displays *C*2 symmetry in solution, with the N of the pyridine ring, the central Co atom and the generated hydride H23 situated in the axis of symmetry. A ddt resonance and doublets integrating to 1H and 2H were located at 8.22 ppm and 8.08 ppm, corresponding to *p*-pyridine and *m*-pyridine protons, respectively. Other resonances integrating to 20H between 7.90 and 7.60 ppm were assigned to the PPh_2 moieties. The full conversion process of $\mathbf{1}^+$ into $\mathbf{2}^{2+}$ in the presence of excess TFSI, monitored by UV/Vis spectroscopy is presented in Figure S22. The absorption spectrum of the final pale orange solution corresponding to the Co^{III}(L)-H species $\mathbf{2}^{2+}$ exhibits two transitions at 297 nm and 379 nm with $\varepsilon \approx 10\,000$ and 5000 M^{-1}cm^{-1}, respectively (blue line in Figure S22).

Elucidation of Hydrogen Evolution Reaction Mechanism

The cobalt hydride species $\mathbf{2}^{2+}$ is stable for several hours under inert conditions in the presence of excess acid source (Figure S16). We attribute the high stability of $\mathbf{2}^{2+}$ to the π-acceptor nature of the phosphine groups of the ligand, which lower the electron density on the metal center anodically shifting the reduction potentials and, therefore, stabilizing the Co^{III}(L)-H species by decreasing its hydricity.[57] The high stability rules out the direct hydrogen evolution through heterolytic or homolytic pathways from Co^{III}(L)-H (B and C in Scheme 1, respectively). Thus, hydrogen should be produced by a reduced Co^{II}(L)-H (D in Scheme 1). Direct formation of Co^{II}(L)-H from reduction of Co^{III}(L)-H with presence of Co^{I}(L) has been observed before for a cobalt complex containing the triphos ligand (triphos = 1,1,1-tris(diphenylphosphinomethyl)ethane)[13] but this reaction is ruled out in the present case as both species are stable in solution for prolonged reaction times (> 14 h, see Figure 3a). Indeed, the process is not thermodynamically feasible considering the redox chemistry of the two species, where $E^2(Co^{III/I}) > E^1(Co^{II/I}\text{-H})$ (Figure 2).

A strong reducing agent, that is, decamethyl-cobaltocene ($CoCp^*_2$, $E_{1/2} = -1.91$ V vs. Fc/Fc$^+$ in MeCN),[58] was used to generate the one-electron reduced species from $\mathbf{2}^{2+}$, as follows. First, pure Co^{III}(L)-H, $\mathbf{2}^{2+}$, was prepared in situ in CD_3CN solution by reacting $\mathbf{1}^+$ with 1 equiv of TFSI acid. The ^{1}H and ^{31}P{^{1}H} NMR spectra in Figure S12 and S13 show the complete transformation from Co^{I}(L) to Co^{III}(L)-H, as expected. Then, 1 equiv of $CoCp^*_2$ was added in three batches to the former mixture. As shown in Figure 4a, the signals of the Co^{III}(L)-H in the ^{1}H NMR spectra gradually disappear with the addition of $CoCp^*_2$ what is concomitant with the growing of new resonances, confirming that the Co^{III}(L)-H derivative is converted to a new diamagnetic species after reacting with the reducing agent. A close examination and comparison of the new spectrum shows that it is the same as that of the parent Co^{I}(L), complex $\mathbf{1}^+$ (Figure 4b). The same conclusion can also be extracted from the ^{31}P{^{1}H} NMR spectra, where the peak at 36.5 ppm from Co^{III}(L)-H decreases upon adding $CoCp^*_2$ and the characteristic peak at 43.2 ppm from $\mathbf{1}^+$ raises (Figure S14 and S15).

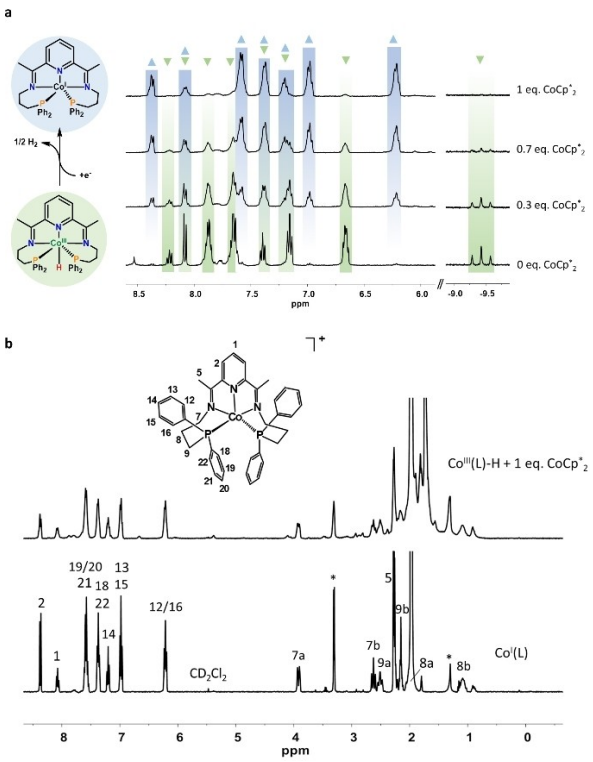

Figure 4. a) ^{1}H NMR spectra (400 MHz, CD_3CN, 298 K) of Co^{III}(L)-H species, $\mathbf{2}^{2+}$, before (bottom line) and after adding overall 0.3 equiv, 0.7 equiv (middle lines) and 1 equiv of $CoCp^*_2$ (top line), presenting the aromatic region resonances and amplified triplet corresponding to the hydride at −9.43 ppm. ▼ indicates peaks decreasing in intensity from Co^{III}-H, $\mathbf{2}^{2+}$, ▲ indicates growing peaks from Co^{I}(L) species, $\mathbf{1}^+$. b) ^{1}H NMR spectra (400 MHz, CD_3CN, 298 K) of the Co^{I}(L) complex $\mathbf{1}^+$ (bottom line) and the species formed by reacting the Co^{III}(L)-H species $\mathbf{2}^{2+}$ with 1 equiv of $CoCp^*_2$ (top line).

The clean transformation of Co^{III}(L)-H, $\mathbf{2}^{2+}$, to initial Co^{I}(L) complex, $\mathbf{1}^+$, upon reduction with 1 equiv of $CoCp^*_2$ suggests that hydrogen gas must be generated through the so-called homolytic pathway F in Scheme 1. Any other catalytic route, such as the heterolytic pathway E in Scheme 1 would lead to a paramagnetic Co^{II}(L)-S species, which would be unstable towards disproportionation as discussed above. The result of a disproportion process would give rise to a mixture of both Co^{I}(L), $\mathbf{1}^+$, and Co^{III}(L)-S, $\mathbf{3}^{3+}$, species as indicated with the grey dotted arrows of Scheme 1, both fully characterized by NMR spectroscopy (Figure S1 and Figure S7). As clearly shown in the top of Figure 4b, a unique product that coincides with pure Co^{I}(L) complex, $\mathbf{1}^+$, appears in the spectrum, supporting the homolytic pathway. In order to check the formation of H_2

through the proposed homolytic pathway, the experiment was repeated by mixing once more $\mathbf{1}^+$ with a strict stoichiometric amount of TFSI followed by $CoCp^*_2$ and the headspace was analyzed by gas chromatography coupled to a thermal conductivity detector (CG-TCD) confirming the immediate formation of H_2 gas upon addition of the reducing agent (Figure S23). The formation of hydrogen in the absence of an extra equivalent of H^+ confirms the involvement of a homocoupling H_2 formation mechanism F in Scheme 1. These results are relevant since homocoupling H_2 formation involves a bimolecular reductive elimination, which in principle should be favored by higher oxidation states in the metal center or by unimolecular intramolecular pathways.[32,33,38–40] Thus, metal-hydride species in III oxidation states (M^{III}-H) have shown to undergo bimolecular pathways for H–H bond formation, invoking certain radical character in the H atom responsible for the coupling. On the other hand, one-electron reduced homologues remain stable against bimolecular coupling and, instead, normally behave as good hydride donors.[34] In sharp contrast, for complex $\mathbf{1}^+$ the Co^{III}(L)-H remains stable while its reduced derivative is the one allowing the reductive elimination towards H_2 formation. We attribute the incapability of the Co^{III}(L)-H species to undergo radical coupling to the high cationic overall charge of the complex responsible for a significant kinetic barrier due to electrostatic repulsions. DFT calculations provided important insights into the electronic structure of the reduced intermediate derived from Co^{III}(L)-H. We found that this species features a doublet electronic structure, where the SOMO spin density is delocalized over the Co d_{z^2} orbitals, the bis(imino)pyridine ligand and the hydride, evidencing its active role in the HER catalysis (Figure S31). With this result, we conclude that contribution of the ligand-based orbitals to the stabilization of reduced oxidation states allows to access reactive intermediates required for hydrogen evolution (i.e., Co^{II}(L)-H). Moreover, the partial contribution of hydride-centered orbitals to the SOMO suggest its proclivity to undergo bimolecular H–H bond formation.

Thus, the proposed complete catalytic pathway towards the formation of molecular hydrogen from organic acids catalyzed by $\mathbf{1}^+$ is summarized in Figure 5. It starts with the generation of the key Co^{III}(L)-H hydride intermediate from the initial Co^{I}(L) compound that reacts with a proton. This species is stable and needs a further $1e^-$ reduction to form the corresponding Co^{II}(L)-H species, which is very reactive and releases H_2 through a homolytic pathway regenerating the initial Co^{I}(L) compound, $\mathbf{1}^+$, closing the catalytic cycle. Hydrogen evolution from the Co^{II}-H or Co^{II}(L)-H species is proposed for several cobalt catalysts reported in the literature but most of the examples undergo heterolytic pathways by reaction with protons in the medium, yet this is highly dependent on the catalytic conditions including acid strength and concentration (pH in aqueous conditions), concentration of catalyst as well as the reaction activation process (electrochemically vs photochemically induced reactions).[5,7,13,15,21] Importantly, the stoichiometric experiment between the Co^{III}(L)-H species, $\mathbf{2}^{2+}$, and the reducing agent $CoCp^*_2$, unequivocally prove the feasibility of generating hydrogen at the Co^{III}(L)-H/Co^{II}(L)-H reduction potential ($E_{onset} = -1.6$ V, Figure 2).

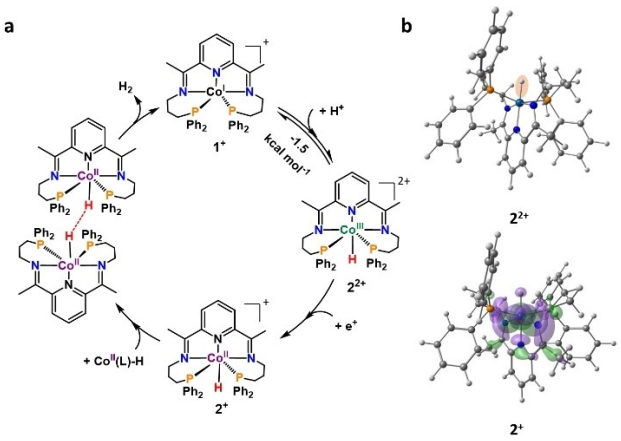

Figure 5. a) Proposed homocoupling catalytic cycle for $\mathbf{1}^+$. Free energy changes are indicated as black number in kcal mol^{-1} and calculated redox potential in volts vs NHE. b) Calculated structures of $\mathbf{2}^{2+}$ and $\mathbf{2}^+$ species with a representation of the SOMO localized in the ligand π-orbitals.

Conclusion

The Co complex $\mathbf{1}^+$ containing a κ-N_3P_2 pentadentate ligand that is based on the redox active 2,6-bis(imino)pyridine scaffold and two phosphine arms, has been successfully prepared. It is formally a Co^I complex, which adopts pseudo trigonal-bipyramidal geometry in the solid state (XRD) and C_2 symmetry in solution (NMR). Complex $\mathbf{1}^+$ is stable under air in the solid state thanks to the π-accepting character of the two phosphine ligands, which stabilize the low valent metal center. Cyclic voltammetry analysis in acetonitrile shows two redox couples at $E^1_{1/2} = -2.02$ V and $E^2_{1/2} = -0.24$ V vs. Fc/Fc^+ that have been assigned to the one-electron ligand-based reduction $Co^I(L^{\bullet -})/Co^I(L)$, and to the two-electron Co^{III}(L)-S/Co^I(L) couple, respectively. The two-electron nature of the $Co^{III/I}$ oxidation underlines the capacity of the Co^{II}(L)-S species to disproportionate and accounts for the isolation of the Co^I(L) derivative in the synthetic process, even though a Co^{II} precursor is used as starting material.

Cyclic voltammetry experiments in the presence of organic acids together with complementary spectroscopic analysis demonstrate the involvement of a Co^{III}(L)-H species, $\mathbf{2}^{2+}$, and its reduced homologue in electrochemically induced HER. Compound $\mathbf{2}^{2+}$ is generated by protonation of the Co^I(L) complex $\mathbf{1}^+$ and its formation is dependent on the acid source strength achieving full conversion with TFSI in acetonitrile solution.

The hydride species $\mathbf{2}^{2+}$ is stable under inert conditions and in the presence of $\mathbf{1}^+$ since they both co-exist in solution over a timescale of hours. On the other hand, by using stoichiometric amounts of a strong reducing agent, $CoCp^*_2$, the Co^{III}(L)-H species is reduced and cleanly transformed

into the initial $\mathbf{1}^{+}$. This transformation, when put in context within the HER mechanism scenario of Scheme 1, implies an homolytic pathway from a Co^{III}(L)-H derivative compound, leading to fast electrocatalysis at $E_{onset} = -1.6$ V vs. Fc/Fc^{+}. Computational characterization of the species able to promote bimolecular HER points to an active Co^{III}-hydride complex where the ligand is reduced by one-electron. The redox non-innocence of the ligand importantly decreases the overall charge of the complex and generates a Co^{II}-H species that dimerizes via H–H bond formation.

Overall, the combination of the redox active bis(imino)-pyridine moiety together with the π-acceptor character of the phosphine ligands provide a unique redox behavior to the cobalt complex, $\mathbf{1}^{+}$, key to access low valent Co and Co–H complexes suitable for HER catalysis.

Acknowledgements

A. Llobet gratefully acknowledge the support from Ministerio de Ciencia, Innovacion y Universidades, and FEDER (PID2019-111617RB-I00), AGAUR 2017-SGR-1631, Ministerio de Ciencia e Innovacion for a SeveroOchoa Excellence Accreditation, Grant No. 2020–2023 (CEX2019-000925-S, MIC/AEI). X. Sala and J. García-antón gratefully acknowledge the Ministerio de Ciencia, Innovacion y Universdades, and FEDER (PID2019-104171-RB-I00). X. Sala thanks ICREA for the ICREA Academia award 2020. B. Jiang is grateful for China Scholarship Council (CSC) Grant, CSC NO. 201406300134.

Conflict of Interest

The authors declare no conflict of interest.

Data Availability Statement

The data that support the findings of this study are available from the corresponding author upon reasonable request.

Keywords: Catalysis · Hydrogen Evolution Reaction · Ligands · Molecular Catalysis · Reaction Mechanism

[1] V. Artero, M. Chavarot-Kerlidou, M. Fontecave, *Angew. Chem. Int. Ed.* **2011**, *50*, 7238–7266; *Angew. Chem.* **2011**, *123*, 7376–7405.
[2] V. S. Thoi, Y. Sun, J. R. Long, C. J. Chang, *Chem. Soc. Rev.* **2013**, *42*, 2388–2400.
[3] J. R. McKone, S. C. Marinescu, B. S. Brunschwig, J. R. Winkler, H. B. Gray, *Chem. Sci.* **2014**, *5*, 865–878.
[4] R. S. Khnayzer, V. S. Thoi, M. Nippe, A. E. King, J. W. Jurss, K. A. El Roz, J. R. Long, C. J. Chang, F. N. Castellano, *Energy Environ. Sci.* **2014**, *7*, 1477–1488.
[5] N. Queyriaux, R. T. Jane, J. Massin, V. Artero, M. Chavarot-Kerlidou, *Coord. Chem. Rev.* **2015**, *304*, 3–19.
[6] W. T. Eckenhoff, *Coord. Chem. Rev.* **2018**, *373*, 295–316.
[7] L. Tong, L. Duan, A. Zhou, R. P. Thummel, *Coord. Chem. Rev.* **2020**, *402*, 213079.
[8] J.-W. Wang, K. Yamauchi, H.-H. Huang, J.-K. Sun, Z.-M. Luo, D.-C. Zhong, T.-B. Lu, K. Sakai, *Angew. Chem. Int. Ed.* **2019**, *58*, 10923–10927; *Angew. Chem.* **2019**, *131*, 11039–11043.
[9] J. L. Dempsey, B. S. Brunschwig, J. R. Winkler, H. B. Gray, *Acc. Chem. Res.* **2009**, *42*, 1995–2004.
[10] P. Du, J. Schneider, G. Luo, W. W. Brennessel, R. Eisenberg, *Inorg. Chem.* **2009**, *48*, 4952–4962.
[11] J. L. Dempsey, J. R. Winkler, H. B. Gray, *J. Am. Chem. Soc.* **2010**, *132*, 1060–1065.
[12] J. L. Dempsey, J. R. Winkler, H. B. Gray, *J. Am. Chem. Soc.* **2010**, *132*, 16774–16776.
[13] S. C. Marinescu, J. R. Winkler, H. B. Gray, *Proc. Natl. Acad. Sci. USA* **2012**, *109*, 15127–15131.
[14] P. Zhang, P.-A. Jacques, M. Chavarot-Kerlidou, M. Wang, L. Sun, M. Fontecave, V. Artero, *Inorg. Chem.* **2012**, *51*, 2115–2120.
[15] S. Varma, C. E. Castillo, T. Stoll, J. Fortage, A. G. Blackman, F. Molton, A. Deronzier, M.-N. Collomb, *Phys. Chem. Chem. Phys.* **2013**, *15*, 17544.
[16] E. S. Wiedner, J. A. S. Roberts, W. G. Dougherty, W. S. Kassel, D. L. Dubois, R. M. Bullock, *Inorg. Chem.* **2013**, *52*, 9975–9988.
[17] A. Rodenberg, M. Orazietti, B. Probst, C. Bachmann, R. Alberto, K. K. Baldridge, P. Hamm, *Inorg. Chem.* **2015**, *54*, 646.
[18] A. Lewandowska-Andralojc, T. Baine, X. Zhao, J. T. Muckerman, E. Fujita, D. E. Polyansky, *Inorg. Chem.* **2015**, *54*, 4310.
[19] P. Huo, C. Uyeda, J. D. Goodpaster, J. C. Peters, T. F. Miller III, *ACS Catal.* **2016**, *6*, 6114–6123.
[20] D. Moonshiram, C. Gimbert-Suriñach, A. Guda, A. Picón, C. S. Lehmann, X. Zhang, G. Doumy, A. M. March, J. Benet-Buchholz, A. Llobet, S. Southworth, *J. Am. Chem. Soc.* **2016**, *138*, 10586–10596.
[21] S. Grau, M. Schilling, D. Moonshiram, J. Benet-Buchholz, S. Luber, A. Llobet, C. Gimbert-Suriñach, *ChemSusChem* **2020**, *13*, 2745.
[22] M. Fang, E. S. Wiedner, W. G. Dougherty, W. S. Kassel, T. Liu, D. L. Dubois, R. M. Bullock, *Organometallics* **2014**, *33*, 5820–5833.
[23] B. H. Solis, S. Hammes-Schiffer, *Inorg. Chem.* **2011**, *50*, 11252–11262.
[24] J. T. Muckerman, E. Fujita, *Chem. Commun.* **2011**, *47*, 12456–12458.
[25] B. H. Solis, S. Hammes-Schiffer, *Inorg. Chem.* **2014**, *53*, 6427–6443.
[26] M. E. Carroll, B. E. Barton, T. B. Rauchfuss, P. J. Carroll, *J. Am. Chem. Soc.* **2012**, *134*, 18843–18852.
[27] W. Wang, M. J. Nilges, T. B. Rauchfuss, M. Stein, *J. Am. Chem. Soc.* **2013**, *135*, 3633–3639.
[28] D. Schilter, J. M. Camara, M. T. Huynh, S. Hammes-Schiffer, T. B. Rauchfuss, *Chem. Rev.* **2016**, *116*, 8693–8749.
[29] E. J. Reijerse, C. C. Pham, V. Pelmenschikov, R. Gilbert-Wilson, A. Adamska-Venkatesh, J. F. Siebel, L. B. Gee, Y. Yoda, K. Tamasaku, W. Lubitz, T. B. Rauchfuss, S. P. Cramer, *J. Am. Chem. Soc.* **2017**, *139*, 4306–4309.
[30] X. Yu, C.-H. Tung, W. Wang, *Organometallics* **2017**, *36*, 2245–2253.
[31] C. E. Castillo, T. Stoll, M. Sandroni, R. Gueret, J. Fortage, M. Kayanuma, C. Daniel, F. Odobel, A. Deronzier, M.-N. Collomb, *Inorg. Chem.* **2018**, *57*, 11225–11239.
[32] J. P. Collman, P. S. Wagenknecht, N. S. Lewis, *J. Am. Chem. Soc.* **1992**, *114*, 5665–5673.
[33] J. P. Collman, J. E. Hutchison, P. S. Wagenknecht, N. S. Lewis, M. A. Lopez, R. Guilard, *J. Am. Chem. Soc.* **1990**, *112*, 8206–8208.

[34] Y. Hu, A. P. Shaw, D. P. Estes, J. R. Norton, *Chem. Rev.* **2016**, *116*, 8427–8462.
[35] T. J. Mazzacano, N. P. Mankad, *J. Am. Chem. Soc.* **2013**, *135*, 17258–17261.
[36] S. R. Parmelee, T. J. Mazzacano, Y. Zhu, N. P. Mankad, J. A. Keith, *ACS Catal.* **2015**, *5*, 3689–3699.
[37] U. Koelle, S. Ohst, *Inorg. Chem.* **1986**, *25*, 2689–2694.
[38] N. X. Gu, P. H. Oyala, J. C. Peters, *J. Am. Chem. Soc.* **2018**, *140*, 6374–6382.
[39] N. X. Gu, P. H. Oyala, J. C. Peters, *J. Am. Chem. Soc.* **2020**, *142*, 7827–7835.
[40] D. Inoki, T. Matsumoto, H. Nakai, S. Ogo, *Organometallics* **2012**, *31*, 2996–3001.
[41] J. Evans, J. R. Norton, *J. Am. Chem. Soc.* **1974**, *96*, 7577–7578.
[42] Q. Knijnenburg, S. Gambarotta, P. H. M. Budzelaar, *Dalton Trans.* **2006**, 5442.
[43] M. Ghosh, T. Weyhermüller, K. Wieghardt, *Dalton Trans.* **2010**, *39*, 1996–2007.
[44] J. M. Darmon, S. C. E. Stieber, K. T. Sylvester, I. Fernández, E. Lobkovsky, S. P. Semproni, E. Bill, K. Wieghardt, S. DeBeer, P. J. Chirik, *J. Am. Chem. Soc.* **2012**, *134*, 17125–17137.
[45] A. M. Tondreau, S. C. E. Stieber, C. Milsmann, E. Lobkovsky, T. Weyhermüller, S. P. Semproni, P. J. Chirik, *Inorg. Chem.* **2013**, *52*, 635–646.
[46] T. K. Mukhopadhyay, N. L. MacLean, L. Gan, D. C. Ashley, T. L. Groy, M.-H. Baik, A. K. Jones, R. J. Trovitch, *Inorg. Chem.* **2015**, *54*, 4475–4482.
[47] T. W. Myers, T. J. Sherbow, J. C. Fettinger, L. A. Berben, *Dalton Trans.* **2016**, *45*, 5989–5998.
[48] R. Gueret, C. E. Castillo, M. Rebarz, F. Thomas, M. Sliwa, J. Chauvin, B. Dautreppe, J. Pécaut, J. Fortage, M.-N. Collomb, *Inorg. Chem.* **2019**, *58*, 9043–9056.
[49] H. Ben-Daat, G. B. Hall, T. L. Groy, R. J. Trovitch, *Eur. J. Inorg. Chem.* **2013**, 4430–4442.
[50] M. R. Mena, J.-H. Kim, S. So, H. Ben-Daat, T. M. Porter, C. Ghosh, A. Sharma, M. Flores, T. L. Groy, M.-H. Baik, R. J. Trovitch, *Inorg. Chem.* **2022**, *61*, 6438–6450.
[51] Deposition Number 2193689 (for $\mathbf{1}^{+}$) contains the supplementary crystallographic data for this paper. These data are provided free of charge by the joint Cambridge Crystallographic Data Centre and Fachinformationszentrum Karlsruhe Access Structures service.
[52] X. Hu, B. S. Brunschwig, J. C. Peters, *J. Am. Chem. Soc.* **2007**, *129*, 8988–8998.
[53] C. Costentin, J.-M. Savéant, *Elements of Molecular and Biomolecular Electrochemistry: An Electrochemical Approach to Electron Transfer Chemistry*, 2nd ed., Wiley, Hoboken, **2006**.
[54] G. A. N. Felton, R. S. Glass, D. L. Lichtenberger, D. H. Evans, *Inorg. Chem.* **2006**, *45*, 9181–9184.
[55] C. H. Lee, D. K. Dogutan, D. G. Nocera, *J. Am. Chem. Soc.* **2011**, *133*, 8775–8777.
[56] B. D. McCarthy, D. J. Martin, E. S. Rountree, A. C. Ullman, J. L. Dempsey, *Inorg. Chem.* **2014**, *53*, 8350–8361.
[57] K. M. Waldie, A. L. Ostericher, M. H. Reineke, A. F. Sasayama, C. P. Kubiak, *ACS Catal.* **2018**, *8*, 1313–1324.
[58] N. G. Connelly, W. E. Geiger, *Chem. Rev.* **1996**, *96*, 877–910.

Manuscript received: June 21, 2022
Accepted manuscript online: August 3, 2022
Version of record online: August 24, 2022